Strain-induced magnetization reorientation in epitaxial Cu/Ni/Cu rings

E. C. Corredor, D. Coffey, and M. Ciria[*]

Instituto de Ciencia de Materiales de Aragón, Consejo Superior de Investigaciones Científicas, Zaragoza, Spain and Departamento de Física de la Materia Condensada, Universidad de Zaragoza, Zaragoza, Spain

J. I. Arnaudas

Departamento de Física de la Materia Condensada, Universidad de Zaragoza, Zaragoza, Spain and Laboratorio de Microscopías Avanzadas, Instituto de Nanociencia de Aragón, Universidad de Zaragoza, Zaragoza, Spain

J. Aisa

Departamento de Ingeniería Mecánica, Universidad de Zaragoza, Zaragoza, Spain

C. A. Ross

Department of Materials Science and Engineering, Massachusetts Institute of Technology, Cambridge, Massachusetts, USA

(Received 29 April 2013; revised manuscript received 2 August 2013; published 23 August 2013)

The role of the strain state in epitaxial (001)-oriented Cu/Ni(14 nm)/Cu rings is investigated using a combination of magnetic force microscopy and finite-element calculations. Rings with an external diameter of 3 and 2 μm and linewidth W larger than 400 nm show two different structures: domains with magnetization oriented in the radial direction exist at the inner and outer radius, separated by an area in the interior of the ring consisting of stripe domains with perpendicular magnetization. The former is the sole magnetic structure observed for $W < 400$ nm. Micromagnetic calculations on narrow-linewidth structures indicate that the radial domain-wall structure consists of elliptical Bloch lines with a shorter and longer length along the tangential and radial directions, respectively. Finite-element calculations show that the anisotropic relaxation of the in-plane strain is larger at the ring inner and outer edges than in the interior part of the ring and accounts for the reorientation of the magnetization direction.

I. INTRODUCTION

The influence of strain state on the fundamental properties of materials as diverse as semiconductors, superconductors, multiferroics, and magnetic materials can be appreciated by considering the effects of strain on important electronic, optical, or magnetic properties.[1–4] The strain therefore has become an important parameter for tuning the properties of thin-film systems since films can be grown epitaxially with specific strain states by selecting appropriate substrates. In patterned structures with finite lateral dimensions, the strain state is modified by patterning leading to changes in physical properties compared to a continuous thin film. The strain relaxation thus can become a pathway for the design of elements with spatially inhomogeneous physical properties as a result of the inhomogeneous strain state caused by patterning.

This article focuses on changes in magnetic properties resulting from magnetoelastic anisotropy caused by patterning of a thin-film system. A model system for the study of magnetoelastic effects is the Cu/Ni/Cu(001) structure: the strain induced in the Ni layer by the misfit with the Cu substrate is responsible, through the magnetoelastic (ME) coupling, for the perpendicular (i.e., out-of-plane) anisotropy observed for nickel thicknesses between 2 and 14 nm.[4,5] The magnetocrystalline anisotropy is small, $K_1 = -4.5$ kJ/m^3 for Ni bulk, and, therefore, neglected for the analysis of films with perpendicular magnetization but orients the in-plane easy direction along the $\langle 110 \rangle$ axes in films with in-plane magnetization. These films show low remanence that is due to the swing of the magnetization **M** out of the plane forming domains with a

size below 200 nm.[6] For planar nanowires patterned from such films along the [100] direction, the breaking of the in-plane strain isotropy induces a ME anisotropy that produces a transverse orientation of the in-plane magnetization with respect to the stripe length.[7]

Here we demonstrate the magnetic properties of Ni rings made from epitaxial Cu/Ni/Cu films as a function of the ring width and clarify the internal structure and energy of the domain walls in radially magnetized rings. The study was carried out in a structure with the Ni layer thickness set at 14 nm, a value where the net perpendicular magnetic anisotropy is small[8] and therefore effects due to nonuniform strain states are expected to be dominant. The domain structure in this film with a weak out-of-plane magnetic anisotropy and effective in-plane magnetic anisotropy consist of stripes or maze structures with **M** pointing up and down with respect to the film surface.[9] Strain relaxation occurs normal to the ring edges and favors the in-plane orientation of **M** along the radial direction of the ring, as we observed previously in a narrow ring[9] and stripes.[7] For wide rings this radially magnetized structure coexists with perpendicular stripe domains in the less-relaxed regions of the ring away from the edges, whereas for ring widths below ≈400 nm a fully radial domain configuration is present. Unlike rings made from films with in-plane magnetization, the magnetization reversal proceeds by the nucleation of reverse domains that generate additional DWs in the ring. Micromagnetic calculations indicate that the DWs in these radially magnetized rings are of vortex type resembling Bloch lines with different spatial extent longitudinal and transverse to the ring radius and provide an

estimate of their energy which is related to the arc length of the domains within the rings.

II. EXPERIMENT

The rings were fabricated by subtractive processing of an epitaxial Cu/Ni/Cu film using electron-beam lithography and ion beam etching with a metallic hard mask. Arrays of rings with an outer ring diameter D of 3 and 2 μm and linewidth W varying from 150 to 1200 nm were first fabricated in a bilayer resist stack on a (001)-oriented Cu (5nm)/Ni (14 nm)/Cu (100 nm) epitaxial film on a Si (001) wafer using electron-beam lithography. A bilayer film of Cr/Al was deposited by electron-beam evaporation on the resist and lifted off to leave ring-shaped Cr/Al hardmasks, and ion beam etching was used to transfer the pattern into the Cu/Ni/Cu layer in a procedure reported elsewhere.[9] An energy-dispersive x-ray spectroscopy map (not shown) performed on a milled ring showed no trace of nickel outside the masked area and signal from the Cr/Al layers on the ring region, indicating that the mask was not completely eroded and protected the Cu/Ni/Cu structures during the ion etching process. This procedure is analogous to the process used in previous work to obtain arrays of epitaxial nanowires.[7] The magnetic microstructure was imaged by magnetic force microscopy (MFM) in the tapping-lift mode, detecting the phase shift with commercial low moment tips magnetized along the tip axis. The dark and bright contrast originate from the stray fields present at the edges of the rings or due to the formation of domains with out-of-plane magnetization. Effects of the tip stray field on the samples' magnetic structure were monitored by measuring the magnetic signal backward and forward along the x scanning directions and, at times, by scanning along the y direction.

III. RESULTS

Figure 1 shows topographic and magnetic images for rings with $D = 3$ μm and W ranging from 1300 to 250 nm. The images were taken after applying a magnetic field out-of-plane. Rings with $W = 1.3$ and 1.2 μm [Figs. 1(a) and 1(b)] show two different domain structures. In the interior of the ring, a maze structure was observed [see Fig. 1(a)]. The stripe width was about 200 nm, a value similar to that obtained for the unpatterned thin film.[6,9] However, for the region at the edge of the ring, the pattern consisted of alternating dark and bright contrast sectors that we interpret as the stray field due to in-plane domains. These configurations are sketched in Fig. 1(k), where the area with transverse **M** is displayed in white, forming domains with the orientation indicated by the arrows. Thus, in the MFM images, the stray field generated by narrow rings with transverse magnetization appears with correlated bright and dark contrast at the inner and outer ring edges along the radial direction, and changes of the contrast along the azimuthal direction indicate a domain wall. That observed correlation can be lost in wide rings if a different domain structure exists in the interior of the ring, such as an out-of-plane magnetized region, shown in gray in the thick ring of Fig. 1(k).

The edge contrast was enhanced as W decreased and became visible at the inner edge ring for $W = 1$ μm and below [Figs. 1(c)–1(h)]. For $W = 430$ nm and below, Fig. 1(f), the
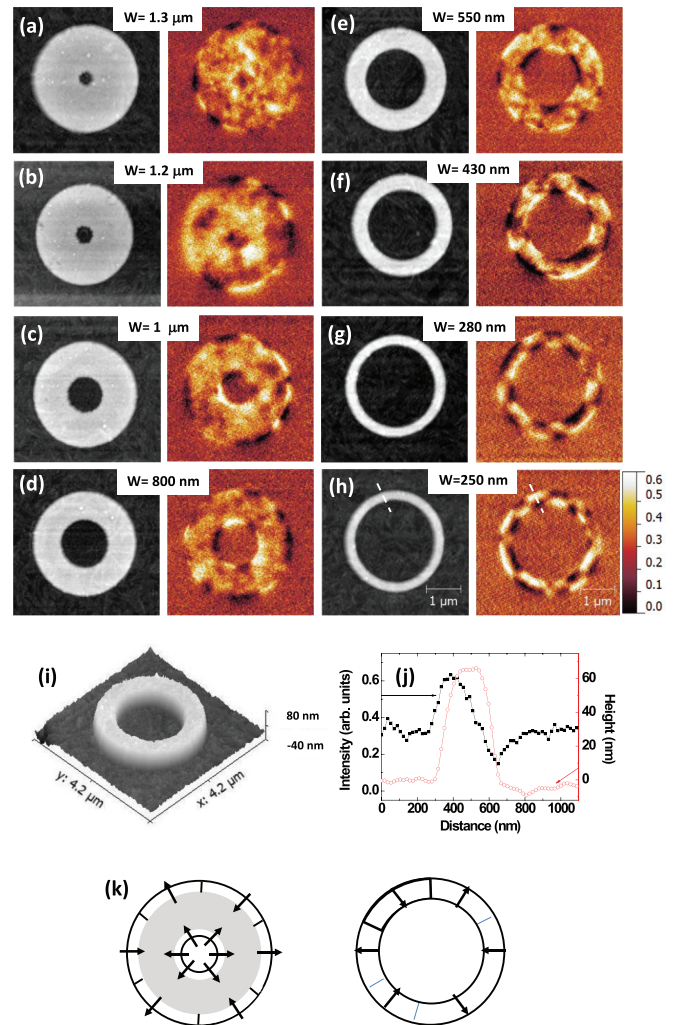

FIG. 1. (Color online) Topographic and phase contrast (magnetic) images of Cu/Ni/Cu rings with a 3-μm external diameter. The rings were scanned at remanence after saturation with an out-of-plane magnetic field. Rings with different widths are shown: (a) 1300 nm, (b) 1200 nm, (c) 1000 nm, (d) 800 nm, (e) 550 nm, (f) 430 nm, (g) 280 nm, and (h) 250 nm. The color scale represents phase shift. (i) 3D topographical representation of the ring with $W = 800$ nm. (j) Profiles taken from the topographic (red) and magnetic (black) signals for the $W = 250$ nm ring along the lines marked in (h). (k) Sketch of **M** at the edges of a wide and a narrow ring. The gray area represents a region magnetized out of plane.

contrast of the inner edge was correlated with the contrast at the external edge such that bright and dark areas appeared at opposite sides of the ring edges. For $W = 280$ and 250 nm [Figs. 1(g) and 1(h)] the domain structure in the middle of the ring width was no longer visible, and the signal varied between bright and dark contrast at the edges.

In Fig. 2, the evolution of the domain structure in the linewidth range $W < 400$ nm is shown for rings with $D = 2$ μm. This follows the same trends as seen in Fig. 1. For the wider ring, $W = 460$ nm, a strong signal at the ring edges and a weak magnetic contrast inside the ring was observed, Fig. 2(a). In narrower rings, Figs. 2(b)–2(f), the edge contrast became dominant and the contrast at the inner and outer edges was correlated in circular sectors. These results clearly
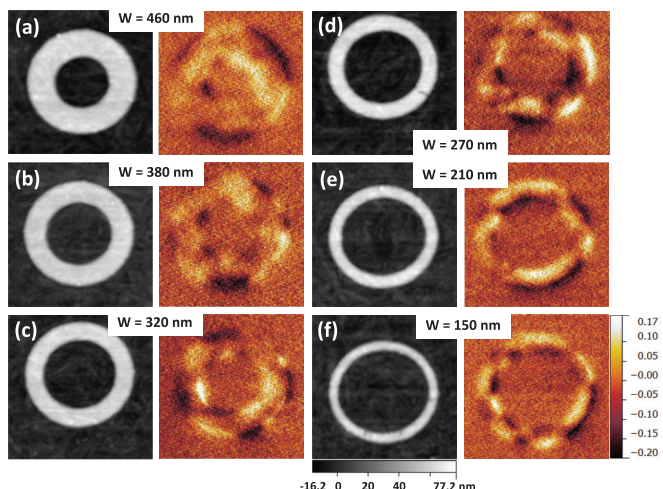
FIG. 2. (Color online) Topographic and magnetic images of Cu/Ni/Cu rings. The sample was imaged at remanence after saturation with an out-of-plane magnetic field. The external diameter was 2 μm and the widths were (a) 460 nm, (b) 380 nm, (c) 320 nm, (d) 270 nm, (e) 210 nm, and (f) 150 nm. The grayscale under (f) shows the height and the color scale on the right shows the phase shift.

indicate the importance of edges in determining the magnetic configuration, and, as linewidth decreased, the edge effects spanned the entire width of the ring.

The edge contrast is attributed to a radial magnetization orientation. Although MFM is not usually a quantitative technique, it was shown that wires with perpendicular magnetization exhibit contrast directly above the magnetic area,[10] while, if **M** is transverse to the wire axis, the stray field has appreciable values away from the edges of the magnetic area.[7] Comparison of the topographical and magnetic images as well as the linescan in Fig. 1(j) shows that the magnetic contrast extended outside the area of the rings. The contrast is characteristic of radial in-plane magnetization, transverse to the ring circumference. The alternating contrast indicates the presence of multiple radial domain walls within the ring.

The dependence of the domain structure on the applied field ranging between -4 kA/m and 32 kA/m is shown in Fig. 3 for a ring with $W = 200$ nm, a linewidth that produced radial magnetization. The field H was applied along the Ni [100] in-plane direction ($\phi = 0$) to first saturate the ring at a negative field of -65 kA/m and then H was increased. At high fields [for example, in the 32-kA/m image or at large negative fields (not shown)], the contrast followed the field direction with dark on one side of the stripe and bright on the other, changing at ($\phi = \pm 90°$), indicating that the ring was at or near in-plane saturation. Close to remanence (-4 kA/m to 2.4 kA/m) the contrast in the first ($\phi = 0°$ to 90°) and third quadrants was still near saturation, but multiple domains appeared in the second and fourth quadrants. Increasing positive field led to the appearance of additional domain walls in the second and fourth quadrants, visible at $H = 8.8$ kA/m and above. The initiation of the reversal of **M** appeared to take place by the generation of domains in some sections of the ring and not by the depinning and movement of the DWs, as was observed in rings with circumferential magnetization that exhibit onion and
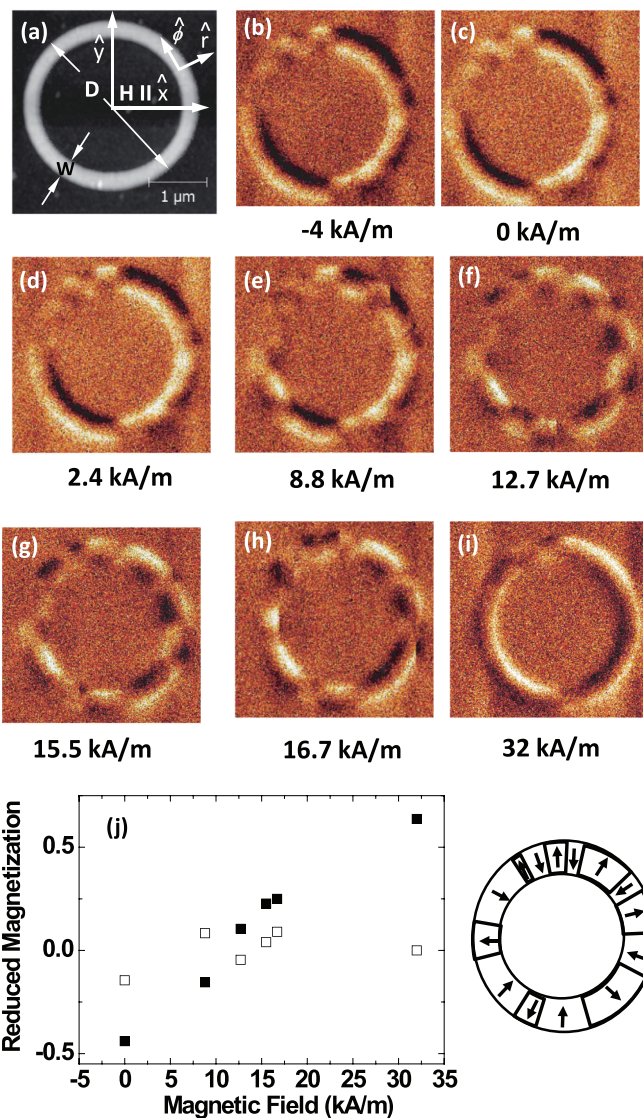

FIG. 3. (Color online) (a) Topographic image or the ring annotated with the geometric parameters. The Cartesian and polar axis as well as the applied field direction are defined. [(b)–(h)] Images of the domain structure during the magnetization process in a ring with $D = 3$ μm and $W = 200$ nm. The field was applied along the Ni [100] in-plane direction and was initially -65 kA/m. Panel (j) displays the magnetization normalized to the total magnetization of the ring along the applied field direction, m_x (solid squares), and along the transverse direction m_y (open squares). A sketch of the magnetic configuration used to calculate m_x and m_y corresponding to (f) is also shown.

vortex states.[11–13] For $H = 16.7$ kA/m, the domains parallel to the field were enlarged by movement of domain walls and, at 32 kA/m, the inversion of the polarity of **M** was nearly complete. The fact that the polarity of the contrast of the ring followed the field direction suggests that the tip magnetization was maintained perpendicular to H and was not demagnetized during the measurements.

The H dependence of the magnetization along the direction parallel, x, and perpendicular, y, to the external applied field, calculated assuming a radially oriented magnetization, is presented in Fig. 3(j) normalized by bulk Ni magnetization,

M_{Ni}, and the ring volume $\pi(D-W)Wt_{Ni}$, namely m_x and m_y. The calculation is done by the integration of $M(\phi)\hat{r}\cdot\hat{x}$ and $M(\phi)\hat{r}\cdot\hat{y}$ over the ring. m_x changed its sign between the configurations at $H=8.8$ and 12.7 kA/m, indicating that the coercive field of the ring was in this range, and a linear extrapolation between these values gave 11.1 kA/m for the coercive field. On the other hand, m_y had values around zero, which are smaller than m_x. The calculated remanence of the ring was about 46% of the total magnetization.

The general MFM contrast of the domain configurations observed at remanence, around the coercive field, and at saturation is similar and supports the interpretation that the ring consisted of domains with high radial remanence and that reversal occurred by the nucleation and propagation of radial domains rather than by rotation of the magnetization. The radial anisotropy in the ring therefore was strong compared to Zeeman, magnetostatic, and magnetocrystalline energies. The ring did show differences in the domain structures between quadrants 1, 3 and 2, 4 at certain fields during the reversal process (Fig. 3), which is indicative of an additional in-plane anisotropy that may be magnetocrystalline or a result of the deposition process, though prior work indicated that magnetocrystalline anisotropy is, in principle, a weak contribution.[9]

IV. DISCUSSION

A. Analytical expression for domain-wall energy

In a previous work[9] we showed that a difference between radial and tangential strain as low as 1.5×10^{-3} is capable, through the ME energy contribution, to overcome the shape anisotropy and favor the transverse (i.e., radial) orientation of **M** in a narrow Ni ring. The ME contribution is given by the expression:[9]

$$\Delta e_{mel}=(B_1\cos^2 2\phi+B_2\sin^2 2\phi)\Delta\epsilon, \qquad (1)$$

where B_1 and B_2 are the ME stress coefficients, ϕ is the azimuthal angle measured with respect to the [100] direction, and $\Delta\epsilon=(\epsilon_{rr}-\epsilon_{\phi\phi})$, with ϵ_{rr} and $\epsilon_{\phi\phi}$ the radial and tangential strain components (in cylindrical coordinates). Here we extend the analysis to the domain structure in narrow rings, assuming that **M** is transverse to the wire axis because it overcomes the magnetocrystalline and magnetostatic energies, to obtain the value of the wall energy density σ_{dw} in the ring. The minimization of the magnetostatic e_{ms} and wall energy per unit volume e_{dw} energies with respect to the domain size Δ provides a relationship between σ_{dw} and measurable quantities as Δ, **M** and the geometrical dimensions of the ring D and W.

The expression for e_{ms} for a ring with two domains was outlined previously.[9] For the case of a ring divided into N domains with identical size, it can be demonstrated, see the appendix, that e_{ms} is given by volume and surface terms, respectively,

$$e_{ms,v}=\frac{1}{2}\mu_0 M^2\frac{1}{\pi(1-\beta^2)\gamma}\sum_{p=1,\,p\text{ odd}}^{\infty}\frac{Q_{v,pN/2}}{p^2}, \qquad (2)$$

$$e_{ms,s}=\frac{1}{2}\mu_0 M^2\frac{1}{\pi(1-\beta^2)\gamma}\sum_{p=1,\,p\text{ odd}}^{\infty}\frac{Q_{s,pN/2}}{p^2}, \qquad (3)$$
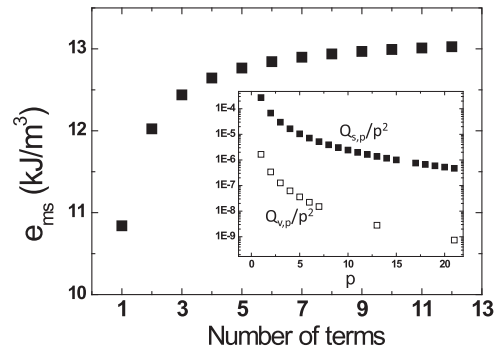

FIG. 4. Calculation of the magnetostatic energy for a ring with $W=200$ nm and $D=3$ μm as a function of the maximum value of the index p of Eq. (2) for a ring with two domains. Inset: Variation of $Q_{s,p}/p^2$ and $Q_{v,p}/p^2$ vs. p.

with

$$Q_{v,n}(\beta,\gamma)=\frac{8}{\pi}\int_{\beta}^{1}dw\int_{\beta}^{1}xdx\int_{0}^{\infty}[J_{n-1}(xy)-J_{n+1}(xy)]$$
$$\times\frac{e^{-\gamma y}+\gamma y-1}{y}J_n(wy)dy, \qquad (4)$$

$$Q_{s,n}(\beta,\gamma)=\frac{8}{\pi}\int_{\beta}^{1}xdx\int_{0}^{\infty}[J_n(y)-\beta J_n(\beta y)]$$
$$\times\frac{e^{-\gamma y}+\gamma y-1}{y}[J_{n-1}(xy)-J_{n+1}(xy)]dy, \qquad (5)$$

where $n=pN/2$, $\beta=1-(2W/D)$, and $\gamma=2t_{Ni}/D$; the J_n are Bessel functions of the first kind that appear because of the cylindrical symmetry of the ring geometry. The sums in Eqs. (2) and (3) run over positive and odd values of p due to the symmetry of the domain configuration. The factor p^{-2} arises from the integration of **M** over the angular variable ϕ. Figure 4 shows $Q_{v,n}/p^2$, $Q_{s,n}/p^2$, and e_{ms} vs. p for a ring with $D=3$ μm and $W=200$ nm and two domains ($N=2$). Because of the factor p^{-2}, it is a reasonable approximation to consider the first five terms in Eqs. (2) and (3) to obtain a value for the magnetostatic energy density used in Fig. 5. Thus, using the first five terms ($p=9$) the value of e_{ms} is 97.5% of the extrapolated value of e_{ms} for large p. Note that for this ring $Q_{v,p}/p^2\ll Q_{s,p}/p^2$ and, therefore, $e_{ms,v}$ is negligible compared with $e_{ms,s}$. The meaning of x, y, and w is explained in the Appendix.

The domain-wall energy per unit volume is the number of domain walls, which is the same as the number of domains multiplied by the wall energy density σ_{dw} and the DW area Wt_{Ni} and divided by the total ring volume. Therefore,

$$e_{dw}=\sigma_{dw}\frac{N}{D}\frac{2}{\pi(1+\beta)}. \qquad (6)$$

Figure 5 shows, for a ring with $W=250$ nm, the dependence of e_{ms} and e_{dw} as a function of the domain size $\Delta=\pi D/N$ for several values of σ_{dw}.

To minimize $e_{dw}+e_{ms}$ with respect to Δ the discrete $e_{ms}(\Delta)$ function was modelled using an extended Langmuir function $ab\Delta^{(1-c)}/[1+b\Delta^{(1-c)}]$, with a, b, and c as constants, because it provides an excellent simulation of the calculated values of
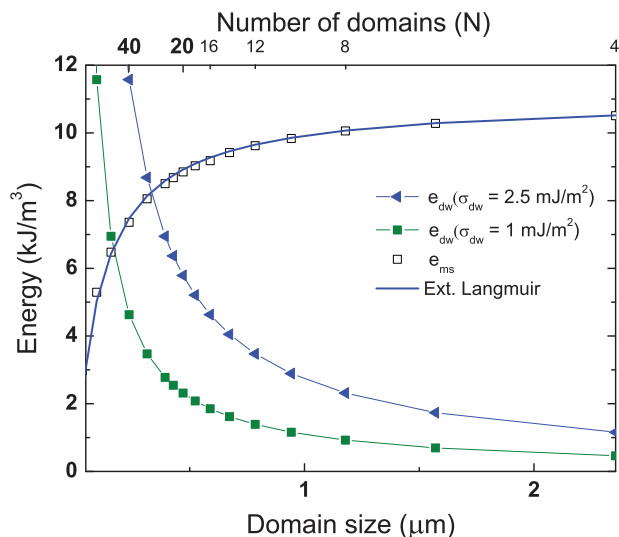
FIG. 5. (Color online) Calculation as a function of the domain size Δ in a ring with $D = 3$ μm and $W = 250$ nm of the domain-wall energy contribution e_{dw} for $\sigma_{dw} = 1$ mJ/m^2 and 2.5 mJ/m^2, the magnetostatic energy e_{ms}, and the extended Langmuir function (thick continuous line) used to simulate e_{ms} with $a = 11\,000$, $b = 1.05 \times 10^{-7}$, and $c = -0.01$. The upper axis shows the corresponding number of domains N.

e_{ms}; see Fig. 5. Thus, an expression for σ_{dw} is obtained,

$$\sigma_{dw} = \frac{1}{2} ab(1-c)(1+\beta) \frac{\Delta^{(2-c)}}{[1 + b\Delta^{(1-c)}]^2}. \quad (7)$$

To estimate Δ (or N), the domain structures imaged by MFM were used. We assume that the differences in the sizes of these domains are due to difficulty in generating domain walls at the ring edges, and thus, the smaller domain size is close to the value of the domain length in the configuration that minimizes $e_{dw} + e_{ms}$. Then, using the image of Fig. 1(h) for a ring with $W = 250$ nm, examination of the smaller domains gives values of N between 16 and 22, and, by minimizing the energy, this corresponds to a value of $\sigma_{dw} \approx 1.23$ mJ/m^2 for $N = 16$ and 1.10 mJ/m^2 for $N = 22$. Assuming $\sigma_{dw} = 4\sqrt{KA}$ with K the effective anisotropy and A the exchange constant ($= 9 \times 10^{-12}$ J/m) and using for σ_{dw} the average value of 1.16 mJ/m^2 a value of ≈ 9.3 kJ/m^3 is obtained for K. This result is in the range of values obtained by evaluation of the effective magnetic anisotropy needed to obtain M transverse to the ring. Evaluating the DW width as $\delta_{dw} = \pi\sqrt{A/K}$, the value obtained is $\delta_{dw} \approx 98$ nm.

B. Micromagnetic calculation

The contribution of the volume charges to e_{ms} is two orders of magnitude smaller than that due to surface charges, and, therefore, the magnetostatic energies of the ring studied in the previous section and of a straight strip of Ni have the same origin. Thus, the simplicity of wire geometry to carry out calculations was used to evaluate the domain structure using a Landau-Lifshitz-Gilbert micromagnetic solver.[14] The strip was 8 μm long, 180 nm wide, and 10 nm thick, with $2.5 \times 2.5 \times 10$ nm unit cells and 0.5 for the Gilbert damping parameter and typical Ni material parameters: saturation

magnetization $M_s = 4.90 \times 10^5$ A/m and exchange constant $A = 9 \times 10^{-12}$ J/m. The relevant contributions to the magnetic anisotropy energy were split into a transverse to the wire term $K_t\sin^2\theta_t$, with θ_t the angle that forms **M** and the transverse direction to the wire axis and $K_t = B_1(\epsilon_{xx} - \epsilon_{yy})$, and $K_p\sin^2\theta_p$ with θ_p the angle that forms **M** and the film normal and $K_p = -B_1[\epsilon_{zz} - (1/2)(\epsilon_{xx} + \epsilon_{yy})]$. We use $K_t = 30$ kJ/m^3 and $K_p = 120$ kJ/m^3, respectively, for the transverse to the wire and perpendicular to the plane anisotropy constants. K_t clearly exceeded the magnetostatic anisotropy energy calculated for the wire. We note that by increasing K_t by the amount of the angular variation of the ME energy in the Ni ring [see Eq. (1)], we affected the domain size and domain-wall geometry in only a minor way. K_p depends on the strain state and a decrement with respect to the unpatterned film has been observed.[7] The value used here is roughly 75% of the value obtained for the unpatterned 10-nm-thick Ni film from the strain measured by x-ray diffraction.

With these parameters a micromagnetic structure with transverse domains was obtained, Fig. 6(a), with a separation between DWs of about 300 nm and $\Delta \approx 1.6$ W. This value would correspond to the minimum DW spacing observable in the MFM image since defects can pin DWs and preclude the formation of smaller domains. Indeed, the smaller domains in Fig. 1 were between 1.2 and 2 times the ring width, in good agreement with the result of the micromagnetic calculation.

1. Structure and energy of the domain wall

The micromagnetic calculation provides information about the domain-wall structure in a strip with transverse anisotropy. The simulation showed domain walls with both in-plane and out-of-plane structure for **M**: The in-plane component formed an elliptical vortex with the minor axis along the longitudinal direction and the out-of-plane component was greatest at the core of the DW, Fig. 6(b). These walls differ from the usual transverse and vortex walls found in strips with longitudinal magnetization or walls in strips with perpendicular anisotropy: The wall in the present case is a vortex-type wall but the vortex is elliptical due to the transverse anisotropy. The domain-wall width was calculated[15] by evaluating the integral of the perpendicular component of **M** and yielded, respectively, a value of ≈ 35 nm and 85 nm for the longitudinal and transverse directions, see the profiles in Figs. 6(c) and 6(d).

The exchange and magnetostatic energy contributions of the DW were estimated by comparing the energies in the zero field of well-defined reference structures calculated using the micromagnetic simulator. The three reference structures consisted of a configuration with uniform **M** transverse to the wire axis, a similar configuration with uniform transverse **M** but containing a zero-width 180° DW, and a configuration in which **M** formed a single vortex. The results are listed in Table I. The difference between e_{ms} for the zero-length wall and the vortex wall configurations provides an estimate of the magnetostatic energy of the DW, ΔE_{ms}. The differences between the energies of the vortex wall and the uniform state provide an estimate of the exchange energy ΔE_{ex}, perpendicular ΔE_p, and transverse ΔE_t anisotropy energies of the DW. The energy associated with the domain wall in the structure E_{dw} was evaluated as the sum of these energy
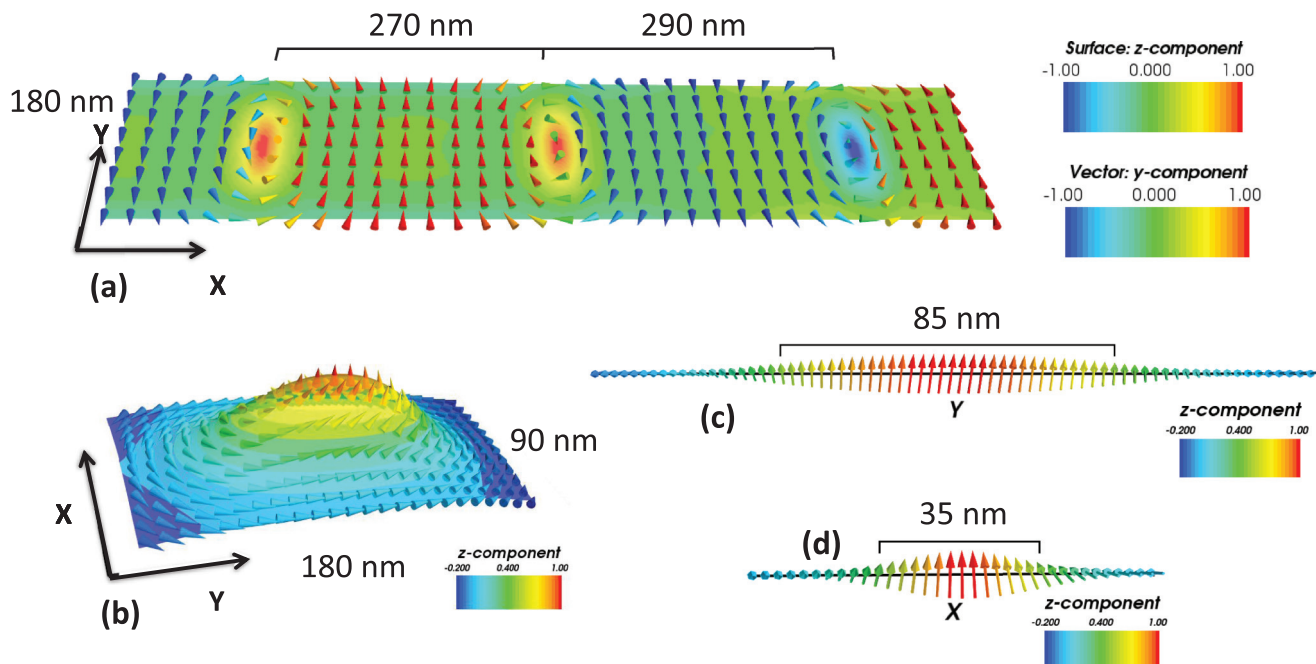
FIG. 6. (Color online) (a) Micromagnetic calculation of the magnetic structure for a wire with the arrows indicating the in-plane magnetization component; (b) detail of the elliptical domain-wall structure; [(c) and (d)] profile of the domain wall along the direction transverse (c) and parallel (d) to the wire axis. For (a) each arrow corresponds to an area of 22.5×22.5 nm^2 while for the rest of the figure each arrow represents an area of 7.5×7.5 nm^2.

differences, which are indicated in Table I. Using $E_{dw} = \sigma_{dw} t_{Ni} W$, $\sigma_{dw} \approx 1.5$ mJ/m^2 ($W = 180$ nm, $t_{Ni} = 10$ nm), a value comparable to the values obtained for σ_{dw} in the previous section. It is worth noting that the presence of an out-of-plane component of **M** in the vortex DW releases energy, ΔE_p is negative, and, as a result, the overall DW energy is decreased.

C. Strain relaxation

The observation of a different domain structure in the middle of the linewidth and at the ring edges for the wider rings suggests that $\Delta\epsilon$ varied along the radius of the ring. An anisotropy in the relaxation of the biaxial in-plane strain of the Ni film ($\approx 0.75\%$ for the film studied here) is required to justify the net radial anisotropy term. To determine this we carried out a finite-element analysis of the strain and stress relaxation in the trilayer Cu/Ni/Cu structure. The initial state

TABLE I. Values of the magnetostatic E_{ms}, the exchange E_{ex}, the perpendicular E_p, and transverse E_t anisotropy energies in a strip with uniform magnetization parallel to the short wire side, a magnetic structure with a single domain wall with zero length, and a vortex domain wall. ΔE_i indicates the values of the different energy contributions to the DW energy calculated as indicated in the text. Units are 10^{-18} J.

	E_{ms}	E_{ex}	E_p	E_t	
M uniform	83.50	0	864.0	0	
Zero length DW	81.86	25.92	864.0	0	
Single vortex DW	81.96	2.14	861.5	2.95	
	ΔE_{ms}	ΔE_{ex}	ΔE_p	ΔE_t	ΔE_{DW}
	0.1	2.14	−2.49	2.95	2.70

included the in-plane epitaxial mismatch strain for the Ni layer in the unpatterned Cu/Ni/Cu structure of 0.75×10^{-2} and the strain were introduced into the model by setting the Ni layer to a temperature at which the thermal expansion of the nickel with respect to the copper was equivalent to the experimental in-plane strain. The resulting stress map distribution for a ring with $D = 1$ μm and $W = 500$ nm is shown in Fig. 7. The image shows a ring quarter and the stress σ along the y Cartesian coordinate; therefore, the σ_{yy} corresponds to the σ_{rr} and $\sigma_{\phi\phi}$ stress when observed, respectively, along the y and x axis. For a ring with $D = 3$ μm and $W = 200$ nm, σ_{rr}, $\sigma_{\phi\phi}$, and $\Delta\sigma = \sigma_{\phi\phi} - \sigma_{rr}$ in the nickel layer along the radial direction are plotted in Fig. 7(a). From the graph and the data, straightforward conclusions can be drawn: (a) σ_{rr} was more relaxed at the edges of the ring that at the center of the linewidth and (b) $\sigma_{\phi\phi}$ is quite uniform, although there was a relaxation in the interior ring area. As a result, $\Delta\epsilon = \epsilon_{rr} - \epsilon_{\phi\phi} = -(\sigma_{\phi\phi} - \sigma_{rr})(1 + \nu)/E$ was calculated with E (=210 GPa) as the Young's modulus and ν (=0.31) the Poisson number; see Fig. 7(c). $\Delta\epsilon$ had its largest values at the edges of the ring linewidth and minimum at the ring center. While for the ring with $W = 200$ $\Delta\epsilon$ had a large value (-6×10^{-3}) at the center of the ring, increasing W implies that the $\Delta\epsilon$ became negligible away from the edges of the ring, and significant values for $\Delta\epsilon$ were observed only at the ring edges.

Thus, from the anisotropic strain, the minimum value of the ME anisotropy, see Eq. (1), can be calculated using the bulk ME coefficients, $B_1 = 6.9$ MPa and $B_2 = 8.9$ MPa.[16] For the ring with $W = 200$ nm the minimum value of $\Delta\epsilon$ of -6×10^{-3} implies that the smaller value of e_{me} is ≈ 41 kJ/m^3, a value larger than the magnetostatic energy of ≈ 13 kJ/m^3, showing that the magnetoelastic anisotropy drove the radial magnetization orientation. For the ring with $W = 1000$ nm
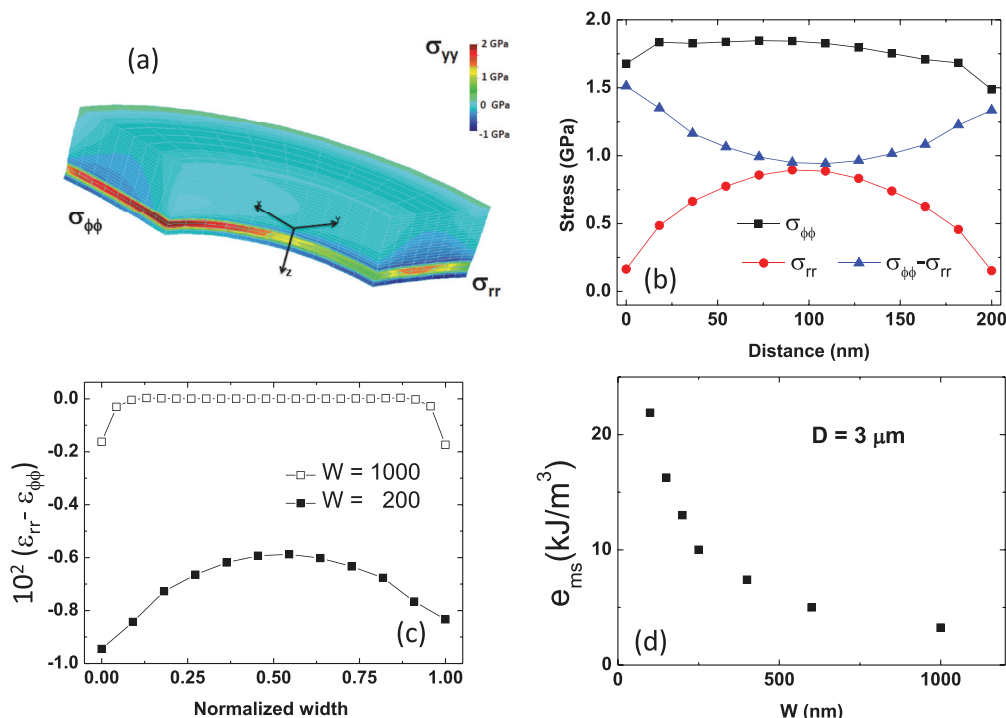
FIG. 7. (Color online) (a) 3D image of the finite-element calculation of the stress σ_{yy} in a Cu/Ni/Cu trilayer ring. The stress in concentrated in the Ni layer near the bottom of the simulation. (b) Profiles of $\sigma_{\phi\phi}$, σ_{rr}, and $\sigma_{\phi\phi} - \sigma_{rr}$ stresses for a ring with $D = 3$ μm and $W = 200$ nm; (c) $\epsilon_{rr} - \epsilon_{\phi\phi}$ for rings with $D = 3$ μm and $W = 200$ nm and 1000 nm. $x = 0$ corresponds to the inner diameter. (d) e_{ms} as a function of W for a ring with $D = 3$ μm.

$\Delta\epsilon$ was zero in the center of the ring width but, at the edges, its value was $\approx -1.5 \times 10^{-3}$, thus, e_{me} had a minimum value of 8.3 kJ/m^3; this value is large enough to overcome $e_{ms} < 3.25$ kJ/m^3. Note that e_{ms} decreased considerably as W increased above 300 nm, Fig. 7(d).

Therefore, the strain dependence can explain the magnetization orientation and the resulting domain structure: For wide rings **M** is transverse in the regions close to the ring edges and domain structures quite similar to that observed in the unpatterned film are present in the interior area, while for narrow rings **M** is transverse for the complete ring.

The strain-induced reorientation observed in the Cu/Ni/Cu systems differs from that reported in rings and planar nanowires of Ti/CoCrPt (10–20 nm)/Ti.[17] In the latter system, **M** reoriented from perpendicular to the film to transverse to the wire and then parallel to the wire axis as the linewidth decreased, without a coexistence of areas with in-plane and out-of-plane orientation of **M**. For the CoCrPt films the perpendicular anisotropy is due to the crystal orientation of the hexagonal c axis normal to the film plane, resulting in a strong magnetocrystalline anisotropy, which does not change on patterning,[18] whereas for the Ni films in this study the magnetocrystalline anisotropy is weak and the ME anisotropy and the shape anisotropy are the dominant contributors to the magnetic anisotropy.

V. SUMMARY

The magnetic domain structure of Cu/Ni/Cu rings with external diameter D of 3 and 2 μm and linewidth W ranging between 100 and 1300 nm is presented. Two regimes are observed at remanence after out-of-plane saturation: For rings with $W > 400$ nm, the contrast at the edges and in the bulk of the ring differed, indicating the presence of a magnetization reorientation along the radial direction. For $W < 400$ nm the domain pattern consisted of homogeneous regions with the magnetization oriented along the radial direction. For the narrower rings subject to an in-plane field, the magnetization reversed by the generation of multiple domains. Further increment of the field produced a movement of DWs that reduced the area of domains with high Zeeman energy.

A finite-element stress-strain calculation shows that the value of the anisotropic in-plane strain is strongly dependent on the ring linewidth, increasing as W decreases, and also having a strong radial dependence for larger W. This leads to a radially oriented magnetization for narrow rings, and a radial orientation near the edges of wide rings which occurs when $\Delta\epsilon$ is large enough to overcome e_{ms}. The regions of radial magnetization are separated by vortex-type domain walls which differ from those existing in strips with axial or perpendicular magnetic anisotropy. The energy of the walls, calculated from a micromagnetic model, is consistent with the value estimated analytically by minimizing the magnetostatic and domain-wall energies over the ring.

The study showed that the ME anisotropy energy drives the spin reorientation in the ring, profoundly affecting the domain structure and reversal process, and enables structures to be made with uncommon domain structures and domain-wall configurations. The selection of a material with

appropriate ME coefficients provides tools for engineering different domain configurations in crystalline wires and rings depending on their orientation with respect to the strain direction. Domain walls between regions of transverse magnetization may be of interest for spin torque transfer measurements or domain-wall devices.

APPENDIX: CALCULATION OF THE MAGNETOSTATIC ENERGY FOR A RING WITH *N* DOMAINS

Equations (2) and (3) are obtained by the calculation of the magnetostatic potential $U(\mathbf{r})$ and the magnetostatic energy for a ring in cylindrical coordinates assuming that $\mathbf{M}$ has only a radial component. In this appendix the derivation of $Q_{s,n}$ for a domain configuration consisting of radial domains is presented based on a procedure used elsewhere.[19] First, the magnetostatic potential at position $\mathbf{r}$ due to surface charges at position $\mathbf{r}'$, $U_s(\mathbf{r})$ is presented as follows:

$$U_s(\mathbf{r}) = \frac{1}{4\pi}\int_s \frac{\widehat{n}' \cdot \mathbf{M}(\mathbf{r}')}{|\mathbf{r} - \mathbf{r}'|} ds', \qquad (A1)$$

where s' stands for the surface of the ring. The expansion[20]

$$\frac{1}{|\mathbf{r} - \mathbf{r}'|} = \sum_{p=-\infty}^{\infty} e^{-ip(\phi-\phi')}\int_0^{\infty} J_p(kr)J_p(kr')e^{k(z_<-z_>)}dk, \qquad (A2)$$

where J_p are Bessel functions of the first kind and $z_<(z_>)$ are the smaller (larger) of $|z|$ and $|z'|$ is used to evaluate $U_s(\mathbf{r})$. The magnetization of a ring with N radial domains can be described as a periodic square wave function of angle ϕ with angular period $4\pi/N$. The radial component of $\mathbf{M}$ can be expanded in terms of a Fourier series as follows:

$$M_r(\phi) = \sum_{n=1,\,n\text{ odd}}^{\infty} \frac{4M}{\pi n}\sin\left(\frac{nN}{2}\phi\right). \qquad (A3)$$

And $U_s(r,\phi,z)$ becomes

$$U_s(r,\phi,z) = \frac{1}{4\pi}\sum_{n=1,\,n\text{ odd}}^{\infty}\frac{4M}{n\pi}\sum_{p=-\infty}^{\infty} e^{-ip\phi}$$
$$\times \int_0^{2\pi}\sin\left(\frac{nN}{2}\phi'\right)e^{ip\phi'}d\phi'\,f_p(r,z) \qquad (A4)$$

with

$$f_p(r,z) = \int_0^{\infty}dk\,J_p(kr)\times\left[\frac{D}{2}J_p\left(k\frac{D}{2}\right) - \frac{D-2W}{2}\right.$$
$$\left.\times J_p\left(k\frac{D-2W}{2}\right)\right]\int_0^{t_{Ni}}e^{k(z_<-z_>)}dz', \qquad (A5)$$

where $f_p(r,z) = f_{-p}(r,z)$ because of the symmetry conditions of the Bessel functions. Therefore, since

$$\int_0^{2\pi}\sin\left(\frac{nN}{2}\phi'\right)e^{\pm ip\phi'}d\phi' = \pm i\pi\delta_{nN/2,p}, \qquad (A6)$$

U_s can be written as

$$U_s = \frac{2M}{\pi}\sum_{n=1,\,n\text{ odd}}^{\infty}\frac{1}{n}\sin\left(\frac{nN}{2}\phi\right)f_{Nn/2}(r,z). \qquad (A7)$$

Now the calculation of $e_{\text{ms},s}$ requires evaluation of the volume integral,

$$\frac{\mu_0}{2}\int_V \mathbf{M}(\mathbf{r})\nabla U(\mathbf{r})dv = \frac{\mu_0}{2}\int_V M_r(\phi)\frac{\partial U_s}{\partial r}dv, \qquad (A8)$$

where v is the ring volume, therefore,

$$e_{\text{ms},s} = \frac{\mu_0}{2V}\int_0^{2\pi}d\phi\sum_{m=1,\,n\text{ odd}}^{\infty}\frac{4M}{\pi m}\sin\left(\frac{mN}{2}\phi\right)$$
$$\times \sum_{n=1,\,n\text{ odd}}^{\infty}\frac{2M}{n}\sin\left(\frac{nN}{2}\phi\right)$$
$$\times \int_{D/2-W}^{D/2}\int_0^{t_{Ni}}f'_{Nn/2}(r,z)r\,dr\,dz \qquad (A9)$$

with $f'_{Nn/2}(r,z) = \partial f_{Nn/2}(r,z)/\partial r$. Integrating in ϕ,

$$e_{\text{ms},s} = \mu_0\frac{4M^2}{\pi V}\sum_{n=1,\,n\text{ odd}}^{\infty}\frac{1}{n^2}\int_{D/2-W}^{D/2}\int_0^{t_{Ni}}f'_{Nn/2}(r,z)r\,dr\,dz. \qquad (A10)$$

The integration over the variables r and z of $e_{\text{ms},s}$ has been done elsewhere.[19] Using the reduced variables $\beta = 1 - (2W/D)$ and $\gamma = 2t_{\text{Ni}}/D$, $x = r/(D/2)$, $y = k(D/2)$, and $w = r'/(D/2)$ the expression presented for $e_{\text{ms},s}$ is obtained.

---

*ciria@unizar.es

[1] Z.-M. Liao, H.-C. Wu, Q. Fu, X. Fu, X. Zhu, J. Xu, I. V. Shvets, Z. Zhang, W. Guo, Y. Leprince-Wang, Q. Zhao, X. Wu, and A.-P. Yu, Sci. Rep. **2**, 452 (2012).

[2] S. Trommler, R. Hühne, K. Iida, P. Pahlke, S. Haindl, L. Schultz, and B. Holzapfel, New J. Phys. **12**, 103030 (2010).

[3] X. Marti, I. Fina, V. Skumryev, C. Ferrater, M. Varela, L. Fabrega, F. Sanchez, and J. Fontcuberta, Appl. Phys. Lett. **95**, 142903 (2009).

[4] R. Jungblut, M. T. Johnson, J. aan de Stegge, A. Reinders, and F. J. A. den Broeder, J. Appl. Phys. **75**, 6424 (1994).

[5] B. Schulz and K. Baberschke, Phys. Rev. B **50**, 13467 (1994).

[6]S. Hameed, P. Talagala, R. Naik, L. E. Wenger, V. M. Naik, and R. Proksch, Phys. Rev. B **64**, 184406 (2001).

[7]M. Ciria, F. J. Castaño, J. L. Diez-Ferrer, J. I. Arnaudas, B. G. Ng, R. C. O'Handley, and C. A. Ross, Phys. Rev. B **80**, 094417 (2009).

[8]G. Bochi, C. A. Ballentine, H. E. Inglefield, C. V. Thompson, R. C. O'Handley, H. J. Hug, B. Stiefel, A. Moser, and H.-J. Güntherodt, Phys. Rev. B **52**, 7311 (1995).

[9]E. Corredor, D. Coffey, J. I. Arnaudas, C. A. Ross, and M. Ciria, Eur. Phys J. B **86**, 134 (2013).

[10]S. H. Lee, F. Q. Zhu, C. L. Chien, and N. Marković, Phys. Rev. B **77**, 132408 (2008).

[11]J. Rothman, M. Kläui, L. Lopez-Diaz, C. A. F. Vaz, A. Bleloch, J. A. C. Bland, Z. Cui, and R. Speaks, Phys. Rev. Lett. **86**, 1098 (2001).

[12]M.-F. Lai, Z.-H. Wei, C.-R. Chang, J. C. Wu, J. H. Kuo, and J.-Y. Lai, Phys. Rev. B **67**, 104419 (2003).

[13]F. J. Castaño, C. A. Ross, C. Frandsen, A. Eilez, D. Gil, H. I. Smith, M. Redjdal, and F. B. Humphrey, Phys. Rev. B **67**, 184425 (2003).

[14]M. Donahue and D. Porter, *OOMMF Users Guide, Version 1.0* (National Institute of Standards and Technology, Gaithersburg, 1998).

[15]A. Hubert and S. R. Schäfer, *Magnetic Domains: The Analysis of Magnetic Microstructures* (Springer, Berlin, 1998).

[16] E. W. Lee and M. A. Asgar, Proc. R. Soc. A **326**, 73 (1971).

[17]D. Navas, C. Nam, D. Velazquez, and C. A. Ross, Phys. Rev. B **81**, 224439 (2010).

[18]F. Ilievski, C. A. Ross, and G. J. Vancso, J. Appl. Phys. **103**, 07C520 (2008).

[19]P. Landeros, J. Escrig, D. Altbir, M. Bahiana, and J. d'Albuquerque e Castro, J. Appl. Phys. **100**, 044311 (2006).

[20]J. D. Jackson, *Classical Electrodynamics*, 3rd ed. (John Wiley & Sons, New York, 1999).